International Journal of Mass Spectrometry 377 (2015) 393–402

Contents lists available at ScienceDirect

International Journal of Mass Spectrometry

journal homepage: www.elsevier.com/locate/ijms

# Dynamic fluxionality and enhanced CO adsorption in the presence of coadsorbed $H_2O$ on free gold cluster cations

Xiaopeng Xing [a,1], Xi Li [a,2], Bokwon Yoon [b], Uzi Landman [b,**], Joel H. Parks [a,*]

[a] Rowland Institute at Harvard, Harvard University, Cambridge, MA 02142, USA
[b] School of Physics, Georgia Institute of Technology, Atlanta, GA 30332-0430, USA

ARTICLE INFO

*Article history:*
Received 29 March 2014
Received in revised form 24 June 2014
Accepted 1 July 2014
Available online 5 July 2014

**MS 1960 to now.**

*Keywords:*
Quadrupole ion trap
Mass spectrometry
Catalysis
Reaction kinetics
Adsorption
Gold clusters

ABSTRACT

This paper presents mass spectrometry measurements of the saturated adsorption of CO in the presence of coadsorbed $H_2O$ on gas phase gold cluster cations, $Au_n^+$, $n = 3–20$, stored in a quadrupole ion trap. Initial mass spectra obtained at 150 K for specific cluster ion sizes as a function of CO pressure and reaction time, indicate increased CO saturation levels correlated with the coadsorption of background $H_2O$ vapor. Subsequent to these low temperature experiments, measurements were made of CO and $H_2O$ coadsorbed on $Au_6^+$ as a function of reaction time at 300 K. These mass spectra indicate that the reaction rate at constant CO pressure increases by an order of magnitude for a constant $H_2O$ pressure. First-principles density-functional theory calculations in conjunction with the above measurements allowed identification of energy barriers that control dynamic structural fluxionality between adsorption complexes that depends strongly on preadsorbed water. The calculations revealed that in the presence of $H_2O$ the energy barrier for the transition state between ground-state triangular and the incomplete hexagonal isomers of the $[Au_6(CO)_3(H_2O)_2]^+$ complex is reduced to ~0 eV and the exothermicity is increased by 0.43 eV. The theoretical results also identified kinetic pathways exhibiting a transition of the incomplete hexagonal isomer of $[Au_6(ih)(CO)_3(H_2O)_2]^+$ to the final saturated complex, $Au_6(ih)(CO)_4^+$. The energetics and kinetic pathway calculations are consistent with increased formation rates of $Au_6(CO)_4^+$ as observed in mass spectra. The insights gained from these theoretical results not only explain measurements of the CO saturated adsorption on $Au_6^+$ in the presence of water, but also assist in rationalizing coadsorption results obtained over the broader range of cluster size at 150 K.



## 1. Introduction

We begin with a brief historical introduction pertaining to the topic of catalytic reactions driven by gold nanoparticles, intended to relate the present research to results in that field. For a comprehensive background we refer to several available reviews of this subject [1–6].

Observation made in the late 1980s [6–8] about the catalyzed oxidation of CO on supported gold nanoparticles initiated extensive research efforts aimed at uncovering the origins and mechanisms underlying the reactivity and catalytic activity of gold. Initially, the measurements of the catalytic reactivity were made for hemispherical gold particles with diameters of about 4–10 nm deposited on metal oxide surfaces. Further measurements indicated that the level of catalytic reactivity was strongly enhanced by coadsorbed water [9–12]. A decade later, to better understand the nature of the catalytic activity of supported gold particles, investigation of CO oxidation reactions were performed on atomically well-defined surfaces [13]. These measurements associated the catalytic activity with bilayer gold islands of 1–6 nm diameter supported on the surface of $TiO_2$; with special emphasize of the role of periphery sites of these islands. Measurements of the effects of water on these controlled surfaces concluded that the enhancement of catalytic reactivity by $H_2O$ was due to an increased activation of molecular oxygen [14,15].

The development of instrumentation [16] with the capability to soft-land mass selected gold clusters of 1–20 atoms on metal oxide films and apply surface analysis techniques to study cluster–molecule interactions, introduced a new direction to the study of catalytic reactivity. These techniques provided the capability to compare measurements of reactivity with tractable

* Corresponding author. Tel.: +1 617 497 4653; fax: +1 617 497 4627.
** Corresponding author. Tel.: +1 404 894 3368; fax: +1 404 894 7747.
*E-mail addresses:* xingxp@tongji.edu.cn (X. Xing), xi_li@fudan.edu.cn (X. Li), bokwon.yoon@physics.gatech.edu (B. Yoon), uzi.landman@physics.gatech.edu (U. Landman), parks@rowland.harvard.edu (J.H. Parks).
[1] Current address: Department of Chemistry, Tongji University, No. 1239, Siping Road, Shanghai 200092, PR China.
[2] Current address: Department of Environmental Science and Engineering, Fudan University, No. 220, Handan Road, Shanghai 200433, PR China.

http://dx.doi.org/10.1016/j.ijms.2014.07.006
1387-3806/

theoretical models. This direction has been greatly advanced by the development of computational methodologies for first-principles calculations and simulations of the properties and interactions of clusters [17] (metal clusters in particular). Of special relevance to the present study is the demonstrated ability of these calculations to predict the optimal structures of the ground- and isomeric-states of gold clusters [18]. These combined experimental and theoretical investigations resulted in deep insights into the chemical catalytic activity and atomic and electronic structures of surface-supported (mass-selected and soft-landed) and gas-phase (stored in a trap) gold (and other metal) clusters, and, most importantly, the mechanisms, dynamics and pathways of reactions catalyzed by these clusters [4b,19–24]. Pertinent to the investigations reported in the present paper we highlight the following findings from previous work:

(1) The catalytic activity of gold clusters has been theoretically predicted and experimentally measured to be highly dependent on cluster size. In particular, in earlier work [19] on size-selected surface-supported gold clusters it has been theoretically predicted, and experimentally observed, that the catalytic activity of gold clusters emerges in clusters containing about 10 atoms having a three-dimensional structure; indeed in the initial work on magnesia-supported gold clusters the gold octamer has been found to be the smallest size cluster to catalyze the low-temperature oxidation of carbon monoxide to form $CO_2$. This prediction, that has been supported initially by mass-spectrometric temperature programmed reaction measurements in the late 1990s [19], has been confirmed several years later in investigations employing aberration-corrected high-resolution electron microscopy [25]. Here we also highlight investigations aimed at exploring the effect of gold cluster dimensionality on the catalytic activity, and of ways to manipulate the dimensionality of supported gold clusters through controlled preparation of metal-oxide thin-films adsorbed on metal substrates (for example magnesia films on Mo(100) or Ag(100)) [23].
(2) First-principles theoretical simulations have revealed and identified dynamic structural fluxionality as an important contributing factor to the catalytic activity of metal (gold in particular) nanoclusters [4b,20], whereby transition state activation barriers of catalyzed reactions are lowered by structural deformations of the cluster in the course of reaction. The concept of structural cluster fluxionality developed, as discussed above, in the context of surface-supported nanocluster catalysis, has been further investigated in studies of adsorption and reactions of hydrogen and oxygen on gas-phase gold cluster cations [24c]. Particularly pertinent to the current paper is the theoretical prediction, supported by the experimental mass-spectrometric data, pertaining to structural fluxtionality of $Au_6^+$ induced by the adsorption of hydrogen molecules, and resulting in isomerization from a ground-state triangular structure to an incomplete hexagonal one. The theoretical results for hydrogen saturation coverages and reaction characteristics between the coadsorbed hydrogen and oxygen molecules were found to agree with the experimental findings. The joint investigations provided insights regarding hydrogen and oxygen cooperative adsorption effects and consequent reaction mechanisms [24c]. The concept [20] of structural fluxionality of clusters (SF), and dynamical SF (DSF), has been employed in a number of investigations. Examples include: (i) probing the structure of gas-phase metallic clusters via ligation energetics, through the use of measured equilibrium ligand-binding energies and entropies to unambiguously obtain structural information for the sequential addition of $C_2H_4$ to $Ag_m^+$ ($m$ = 3–7) clusters, where it been shown that global structures can be obtained from temperature-dependent equilibrium data. Moreover, the method was found to be sensitive to ligand-induced SF of the clusters [26]; (ii) density functional studies of the reactivity of medium size gold cluster, $Au_n$, ($n$ = 14, 25, 29) with molecular oxygen, showing a strong dependence on SF [27]; photoelectron spectroscopy and first-principles calculations of $[Au_7(CO)_n]^-$ ($n$ = 1–4), exhibiting SF manifested by structural dimensionality crossovers [28]; first-principles investigations of the collision processes between $Au_6^-$ and $Ag_6^-$ clusters and $O_2$, where SF has been found to play an important role, and the higher sticking probabilities of the molecule to the silver anions were attributed to inherently different dynamical processes connected with the higher structural rigidity of $Au_6^-$ vs the floppy-like behavior of $Ag_6^-$[29]; electronic structure investigation of the SF pathways emerging when transition metal anion clusters, $W_3O_6^-$ and $Mo_3O_6^-$, react with hydrogen sulfide and ammonia. This study reported effects on the SF pathway due to different spin states of the anionic metal oxide cluster (doublet vs quartet), and the nature of the nonmetal in the small molecule (O vs S vs N) [30].
(3) Theoretical calculations [22] have uncovered molecular mechanisms of water-induced (low humidity) enhancement of the gold catalyzed combustion of CO, entailing the activation of $O_2$ through formation of an hydroperoxyl intermediate.

The relationship between saturated adsorption and cluster structure has been studied previously in cluster beams for CO on clusters of $Ni_n$ ($n$ = 2–20) [31]. The saturation of $Ni_n(CO)_m$ suggested changes in the geometric structure induced by CO adsorption that could accommodate additional CO molecules. Studies of the adsorption of a single CO on isolated gold cluster cations in a Fourier transform ion cyclotron resonance mass spectrometer enabled measurements of the CO binding energy over a wide range of cluster sizes [32]. Calculations [32] of the $Au_nCO^+$ structures for $n$ = 3–9 found that a single adsorbed CO molecule can result in a different structure of the cluster complex than that corresponding to the lowest energy of the bare cluster. Adsorption studies [33] of gold cation beams combined measurements of saturation adsorption with infrared spectroscopy, aiming at interpretation of the data with the use of quantum-chemical calculations [34]. The data recorded for the gold cation beam, $Au_n^+$ ($n$ = 3–10) [33], suggests that successive adsorption of CO molecules can cause distortion of the cluster structure. The only previous measurements [35] and calculations of the coadsorption of $H_2O$ and CO on free gold clusters have been performed for binary $Ag_nAu_m^+$ cluster cations of very small size ($n+m$ = 3).

In this paper, we present experiments and first-principles density-functional theory (DFT) calculations on mass-selected gas phase gold cluster cations, aiming at understanding the variation of CO saturated adsorption levels observed in the presence of water molecules. In addition, adsorption on gas phase cluster cations provides a well defined experimental configuration to observe and interpret dynamic structural fluxionality, suggested [20] to be a viable mechanism for enhancing reaction rates in nanocatalysis [4b,20].

Initial measurements were made for the saturated adsorption of CO on $Au_n^+$ at 150 K as a function of cluster size over the range of $n$ = 3–20 atoms. These measurements identified interesting changes in the saturation levels introduced by $H_2O$ coadsorption from a residual water background pressure. These low temperature experiments were followed by controlled measurements at 300 K of CO adsorption on $Au_6^+$, with and without the coadsorption of $H_2O$, to aid the interpretation of the dynamics of these processes. Density-functional theory calculations identified the mechanism

of water-assisted reduction of the energy barrier controlling the rate of dynamic structural fluxionality between isomers of the adsorption complexes. These calculations explored also specific kinetic pathways that included desorption of weakly bound $H_2O$ molecules.

Our presentation starts in Section 2 with a description of the experimental setup and theoretical methods. The results for CO adsorbed on $Au_5^+$ and $Au_{16}^+$ at 150 K are presented in Section 3.1, illustrating the way that mass spectra exhibit characteristics of fluxionality and the effects accompanying $H_2O$ coadsorption. Experimental and theoretical results for the coadsorption of CO and $H_2O$ on $Au_6^+$ are described in terms of transitions between adsorption state complexes in Section 3.2. Calculations of transition state (TS) energy barriers corresponding to TS complexes that depend on the number of both CO and $H_2O$ molecules adsorbed on $Au_6^+$ are given in Section 3.2, and kinetic pathways for the transition of the incomplete hexagonal isomer $[Au_6(ih)(CO)_3(H_2O)_2]^+$ to the final saturated complex, $Au_6(ih)(CO)_4^+$, are discussed in Section 3.2.2. A summary of the results is given in Section 4.

## 2. Experimental and theoretical methods

Adsorption experiments were performed on existing instrumentation that is described in more detail elsewhere [18b,36]. The ion trap mass spectrometer presents an excellent opportunity both to isolate a specific ion species and to store a sufficient number of mass-selected ions for a sufficiently long duration to accomplish physical measurements that could not be performed otherwise. The ability to store cluster ions in a reactant gas for extended times allows the adsorption to be measured at lower reactant pressures. As a result, slower adsorption rates can produce mass spectra that clearly exhibit the evolution of adsorption states leading to saturation. This capability helps to follow the development of larger mass peaks related to populations of the more important adsorption structural isomers. Collisions of stored ions with a background helium gas equilibrates kinetic and internal degrees of freedom of the ion cluster at the gas temperature, allowing measurements of ion properties under thermal equilibrium conditions. This issue is exceptionally important when characterizing ion structures and dynamics such as the adsorption of molecules on cluster ions.

### 2.1. Experimental setup

The instrumentation includes a DC magnetron sputter-ion cluster source operating at 77 K that uses high purity gold targets to generate gold cluster cations. The ion beam is first guided into a time-of-flight (TOF) mass spectrometer (mass resolution of >500) that exhibits a spectrum of only singly charged clusters as discussed in the Supplementary data Section S2. The cluster ion beam is then guided into a temperature controlled quadrupole ion trap through an aperture in the endcap electrode. The trap is designed to efficiently mass select a specific cluster size and store $\sim 1–5 \times 10^3$ cluster ions for adsorption measurements. Cluster ions are relaxed to the trap temperature by a 3–5 s helium pulse that is then reduced to a constant helium flow to provide a background gas pressure of $\sim 4 \times 10^{-4}$ Torr that maintains the trapped ion temperature. Reactant gas flows are introduced directly into the trap through Granville-Phillips variable leak valves that controlled each gas flow into the ion trap through independent gas lines. The CO flow is composed of ~2% CO seeded in helium, and the water vapor is seeded in helium by bubbling the helium through a diluted ionized (DI) water reservoir. The CO and helium gases were 99.9999% pure. The helium partial pressure in the trap from these reactant gas lines is negligible ($1 \times 10^{-5}$–$1 \times 10^{-7}$ Torr) compared to the background helium pressure. Pulse valves (General Valves, Series 9) control the reaction time and flow rate independently for each reactant gas. All valves are mounted external to the vacuum system. After a chosen reaction time of ~0.1 s–60 s, the ion distribution inside the trap, composed of metal clusters as well as the reaction products, is analyzed by sequentially ejecting ions into a Channeltron electron multiplier that records the ion mass spectra. Spectra achieve a mass resolution of ~100–200 that is sufficient for our adsorption measurements.

The reactant gas pressures are monitored using a Granville-Phillips ion gauge and a Stanford Research System residual gas analyser (RGA200) external to the ion trap. The initial background pressures for CO and $H_2O$ are $3 \times 10^{-9}$ Torr and $7 \times 10^{-9}$ Torr, respectively, prior to data acquisition for a specific cluster size. The mass spectrum for the bare cluster sizes are obtained at this initial background pressure. During an experimental adsorption run for this cluster size, the background partial pressure of CO or $H_2O$ increases over a range of $0.5–1 \times 10^{-8}$ Torr. The uncertainty of the pressures shown in the figures are only significant (±25–35%) for mass spectra obtained at the lowest reactant partial pressures ($2.4 \times 10^{-8}$ Torr). All other spectra were obtained at reactant pressures increased by factors of 10.

Although reactant gases flow directly into the ion trap, the diameter of the trap apertures and the trap electrode spacings are sufficiently large that the small differences between pressure measurements inside and outside the trap can be neglected. This was verified by measuring the kinetic reaction rate of $Au_n^+$ ($n = 8–10$) with CO at room temperature on this system. The rates obtained using pressures measured outside the ion trap are identical within experimental uncertainty to those previously reported [32] (see Supplementary data Section S3.2).

The adsorption spectra of CO and $H_2O$ on $Au_n^+$ display mass peak lineshapes exhibiting asymmetry, shoulders and small unresolved peaks. The raw data in these experiments were not analytically deconvoluted [37] to reduce these lineshape characteristics. Residual gas analyzer (RGA) spectra were dominated by CO and $H_2O$ peaks and did not detect the presence of impurities consistent with the overall use of high purity practices in these experiments.

The mass peak lineshape characteristics are introduced by the methods used to eject ions [38] from the quadrupole ion trap. For example, we have observed that changing ejection parameters or ejection methods is accompanied by changes in the lineshape characteristics but not the mass peak position, although recalibration is usually required. The additional “peaks” on the high mass side of the bare gold clusters in Fig. S1.1 and S1.2 are not observed in the adsorption spectra because different ejection parameters were used to obtain the spectra of the adsorption complexes. The ejection parameters used to obtain adsorption spectra were routinely changed to ensure that adsorbed CO and $H_2O$ were not desorbed in collisions with the background helium gas occurring during ejection.

Section S3.1 in the Supplemental data indicates that low resolution mass spectra, such as shown in Fig. 2 for $Au_5^+$, are sufficient to assign the mass peaks to specific CO adsorption complexes even in the presence of the lineshape distortions discussed above. Section S.3.2 of the Supplemental data demonstrates that measurement of the formation rate of single CO adsorption on gold cluster cations [32] is also insensitive to large differences in resolution. The ability to assign peak masses and the calculation of formation rates do not require exceptionally high resolution in experiments presented in this manuscript, but does require that the peaks of different adsorption complexes are resolved and that the specific adsorption molecule is known and stable during ejection from the ion trap.

### 2.2. Computational methods

In explorations of the atomic arrangements and electronic structures of gold cluster cations, the binding characteristics and structures of molecules adsorbing on such clusters, and the mechanisms of reactions catalyzed by these clusters, we have used first-principles DFT calculations. In particular, we employed the Born–Oppenheimer (BO) spin density functional (SDF) molecular dynamics (MD) method, BO-SDF-MD, [17a] with norm-conserving soft pseudopotentials (including a scalar relativistic pseudopotential for Au) [39] and the generalized gradient approximation (GGA) [40] for electronic exchange and correlations. In these calculations we have used a plane wave basis with a kinetic energy cutoff of 62 Ry. The BO-SDF-MD method [17a] is particularly suitable for investigations of charged systems since it does not employ a supercell (i.e., no periodic replication of the ionic system is used). Structural optimizations were performed using a conjugate-gradient-like method. Previous investigations of gold clusters (as well as other clusters) and their chemical reactivity using the above methodology have yielded results in good agreement with experimental findings.

In the first-principles calculations of the reaction profiles (pathways and transition state energy barriers), a reaction coordinate was judiciously chosen. The reaction coordinate may consist of several geometrical parameters pertinent for the studied mechanism – for example, a reaction coordinate may entail the distance between two atoms and/or an angle between atoms of the gold cluster, or the distance between a reactant atom and a selected atom, or atoms, of the gold cluster. For each value of the reaction coordinate, the total energy of the system was optimized through unconstrained relaxation of all of the other degrees of freedom of the system (reactant molecules and gold cluster atoms). The reaction profiles were obtained via repeating such calculations for various values of the chosen reaction coordinate. These calculations yield results that are the same as, or close to, those obtained by other methods, e.g., the nudged elastic band and variants thereof; see the discussion on pp 89 and 90 in Ref. [4a].

## 3. Results and discussion

### 3.1. CO adsorption on $Au_n^+$

An overview of the measured saturated adsorption levels of CO on $Au_n^+$ at 150 K over the entire size range ($n$ = 3–20 atoms) is shown in Fig. 1. A value of $m$ is taken as the saturation value if the mass spectrum peak for $m$ does not change for reaction times of 10 s–30 s. The saturation values of $m$ are observed to increase approximately linearly for cluster sizes $n \leq 10$, suggesting a correlation with the increase of the number of adsorption sites

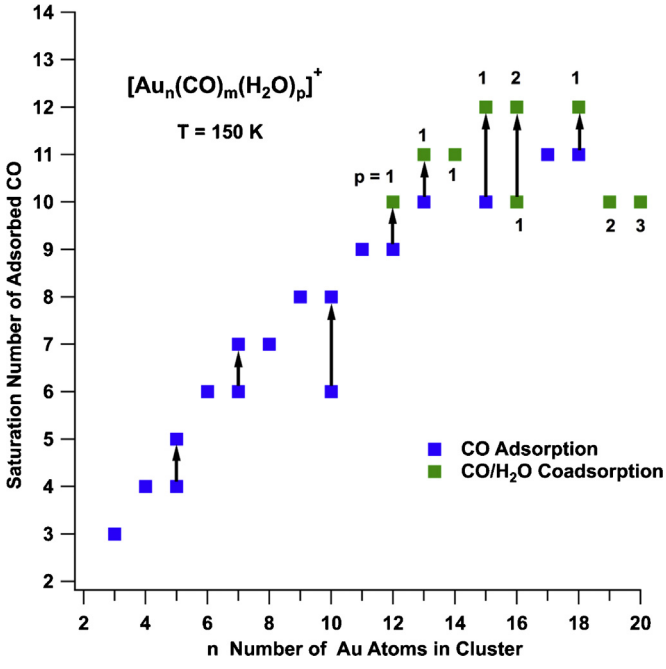


**Fig. 1.** The saturation number ($m$) of adsorbed CO molecules on $Au_n^+$ plotted vs $n$. Blue squares correspond to experiments in which the mass spectra correspond to clusters with only adsorbed CO molecules, whereas the green squares indicate that coadsorption with $H_2O$ is observed. Adsorption of $H_2O$ from the residual background water vapor is described in the text. Arrows indicate transitions occurring between an intermediate adsorption state and the final saturation state. (For interpretation of the references to color in this figure legend, the reader is referred to the web version of this article.)

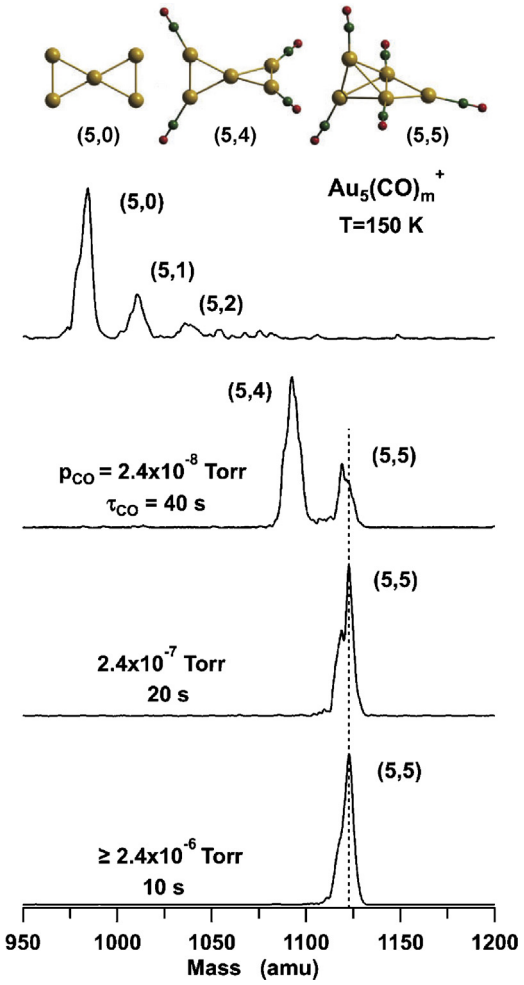


**Fig. 2.** Mass spectra for CO adsorption on $Au_5^+$, shown for various CO pressures and reaction times. Although the $y$-axes have been removed for clarity, the peaks display the relative abundance of parent and product cluster ions. The initial spectrum for bare clusters is obtained at the CO background pressure. Dashed lines align identical adsorption levels in different mass spectra. The mass peaks are denoted with ($n$,$m$) corresponding to $[Au_nCO_m]^+$. The structures shown above the top spectrum correspond to optimal configurations proposed in previous calculations [41], see text. Gold atoms are represented by yellow spheres, oxygen atoms by red spheres, and carbon atoms by green spheres. These structures have been reproduced from Ref. [41] with permission from the PCCP Owner Societies. (For interpretation of the references to color in this figure legend, the reader is referred to the web version of this article.)

on the perimeter of planar (two-dimensional, 2D) cluster isomers [32,34]. For gold cluster ions with $n > 11$ atoms the CO saturation values follow two trends. In one of these trends, indicated by the blue squares in Fig. 1, the slope of saturation values vs $n$ begins to decrease slowly after $n \sim 11$. These values could be associated with CO adsorption on three dimensional, 3D, clusters [34], which may involve coordination of the adsorbed molecule to a larger number of weaker-binding sites compared to the 2D case. On the other hand, the saturation values indicated by the green squares appear to maintain the initial slope vs $n$. Note, however, that these points are saturation values obtained for cluster sizes that coadsorb water as discussed below for $Au_{16}^+$. The arrows in Fig. 1 indicate transitions from an intermediate adsorption state to a final saturation level. The occurrence of this transition is most likely a signature of cluster dynamic structural fluxionality as discussed below for $Au_5^+$.

### 3.1.1. Saturated adsorption on $Au_5^+$

Fig. 2 displays a sequence of mass spectra obtained at 150 K for CO adsorption on the gold pentamer cation, $Au_5(CO)_m^+$ ($m = 0, 1, 2, \ldots$), for several values of CO pressure. The top panel shows the mass spectrum for "closed valve" conditions for which the residual CO pressure in the vacuum chamber is $p_{CO} \approx 3 \times 10^{-9}$ Torr. Even at these low pressures, adsorption occurs for $m = 1$ and 2 for a reaction time of <0.3 s. The spectrum for CO at a pressure of $2.4 \times 10^{-9}$ Torr and a reaction time of 40 s displays only mass peaks for $m = 4$ and 5. The spectrum in the bottom panel displays the saturation value $m = 5$ and similar spectra are obtained for reaction times of 20 s–60 s indicating that this represents an equilibrium state. For increased CO pressures, the saturation peak of $Au_5(CO)_5^+$ is observed independent of pressure and reaction times. As shown in Fig. 2, there can be peaks in the mass spectra, such as the $m = 4$ peak, that dominate the mass distribution prior to the appearance of the final saturation peak. These transients represent intermediate states of saturated adsorption.

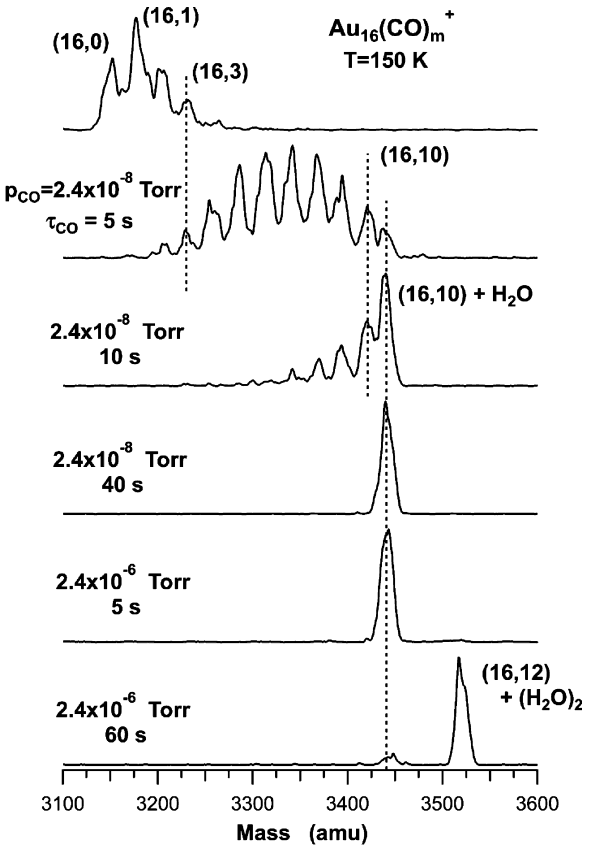


**Fig. 3.** Mass spectra for CO adsorption on $Au_{16}^+$, shown for various CO pressures and reaction times. Although the $y$-axes have been removed for clarity, the peaks display the relative abundance of parent and product cluster ions. The initial spectrum for bare clusters is obtained at the CO background pressure. Adsorption of $H_2O$ from residual background water vapor is described in the text. Dashed lines align identical adsorption levels in different mass spectra. The mass peaks are denoted with ($n$, $m$) corresponding to $[Au_nCO_m]^+$. The mass corresponding to a single adsorbed $H_2O$ molecule is the mass-interval between the two parallel dashed lines marked (16, 10) and (16, 10) + $H_2O$.

Optimal structures for the adsorption complexes $Au_5(CO)_m^+$ ($m = 1$–5) have been reported recently [41]. A similar structure, proposed earlier [32], for $m = 1$, and the structures for $m = 2$–4 indicate sequential adsorption on apex sites [33]. However, the adsorption of a fifth ($m = 5$) CO was found [41] to markedly change the cluster structural motif.

The structures calculated for the bare cluster $Au_5^+$[34,41], $Au_5(CO)_4^+$ and $Au_5(CO)_5^+$ [41] are shown above the mass spectra in Fig. 2. The three dimensional (side-capped) tetrahedral motif proposed for the $[Au_5(CO)_5]^+$ complex [41] has also been found [42] to be part of structures determined for the lowest energy isomers of the anion $[Au_6(CO)_5]^-$ and neutral $[Au_6(CO)_5]$ complexes. Structural similarities to the complex $[Au_5(CO)_4]^+$ are also found in low energy isomers proposed for $[Au_6(CO)_4]^-$ and $[Au_6(CO)_4]$ [42]. These similarities are likely related to the structures found for the ground state isomers of $Au_6^+$ [34] and $Au_6^-$ [34,43], with both charge states having similar structures

The dynamical structural fluxionality [28] that underlies the rearrangement of the structural motif of $Au_5(CO)_5^+$, resulting in the structure shown in Fig. 2, is thus manifested in the mass spectra to occur in the CO pressure range of $\sim 2 \times 10^{-8}$–$\sim 2 \times 10^{-7}$ Torr. The mass spectrum at $p_{CO} = 2.4 \times 10^{-8}$ Torr shows the populations of the two complex structures taking part in the fluxionality. Additionally, the calculated binding energy decreased from 0.81 eV to 0.18 eV over the transition of 4–5 adsorbed CO molecules, and consequently the saturated adsorption for $m = 5$ was observed only below 200 K [41]. The results displayed in Fig. 2 corroborate the previous saturation measurement for $Au_5^+$ in detail.

### 3.1.2. Coadsorption of CO and $H_2O$ on $Au_{16}^+$

The first adsorption data exhibiting the coadsorption of $H_2O$ on $Au_n^+$ are indicated in Fig. 1 for $n \geq 12$. The $[Au_n(CO)_m(H_2O)_p]^+$ complexes are formed by adsorption of $H_2O$ from the background water vapor having a pressure of $p(H_2O) \approx 7 \times 10^{-9}$ Torr in the vacuum chamber during the CO reaction. The mass spectra for clusters with sizes $n = 12, 13, 15, 16$ and 18 display similar dynamics in which the complex formed with the saturated CO level appears only after adsorption of a single $H_2O$ molecule.

The mass spectra for $Au_{16}^+$ at 150 K shown in Fig. 3 display an adsorption spectrum common to other clusters in this larger size range. The spectrum exhibits an intermediate saturation level for the complex $[Au_{16}(CO)_{10}H_2O]^+$ for CO pressure up to $2.4 \times 10^{-6}$ Torr and reaction time of 5 s. Development of the final saturated complex, $[Au_{16}(CO)_{12}(H_2O)_2]^+$, entailing the adsorption of a second $H_2O$ and two CO molecules, occurs after a longer reaction time of 60 s. Similar coadsorption behavior is shown in the Supplementary data for clusters $Au_{12}^+$, $Au_{13}^+$, $Au_{15}^+$ and $Au_{18}^+$.

Whereas we defer a detailed discussion pertaining to the water-assisted dynamical fluxionality mechanism to the next section, it is pertinent to comment here that the correlation of $H_2O$ adsorption with an observed abrupt change in the saturation number, occurring for five larger cluster sizes ($Au_n^+$, $n = 12$–18), suggests strongly the involvement of a structural change in this process. We also recall that a similar abrupt change in the saturation number has been observed for the small $Au_5^+$ cluster,

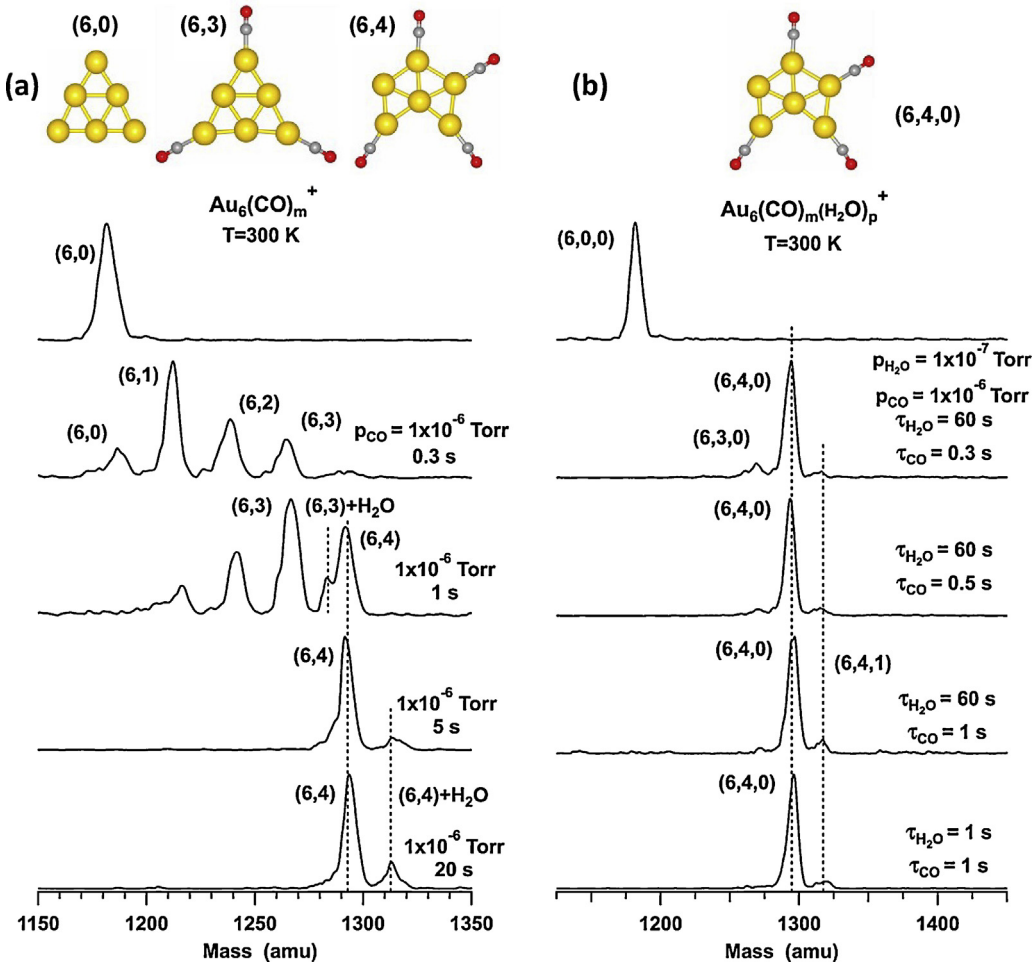


**Fig. 4.** (a) Mass spectra for CO adsorption on $Au_6^+$, shown for various CO pressures and reaction times. Although the *y*-axes have been removed for clarity, the peaks display the relative abundance of parent and product cluster ions. The initial spectrum for bare clusters is obtained at the CO background pressure. Adsorption of $H_2O$ from residual water vapor in the middle spectrum is described in the text. Dashed lines align identical adsorption levels in different mass spectra. The mass peaks are denoted with (6, *m*) corresponding to $[Au_6CO_m]^+$. The optimal structures shown above the top spectra are from theoretical calculations described in the text. Gold atoms are represented by yellow spheres, oxygen atoms by red spheres, and carbon atoms by gray spheres; (b) mass spectra for coadsorption of $H_2O$ and CO on $Au_6^+$, shown for various CO and $H_2O$ pressures and reaction times. The initial spectrum for bare clusters is obtained at the CO and $H_2O$ background pressures. The mass peaks are denoted with (6, *m*, *p*) corresponding to $[Au_6CO_m(H_2O)_p]^+$. Further description is similar to (a). (For interpretation of the references to color in this figure legend, the reader is referred to the web version of this article.)

but without the intervention of $H_2O$ in the saturated adsorption complex (see previous section). It is possible that the stronger binding energy of CO on smaller clusters [32,41], e.g., $Au_5^+$, releases sufficient energy to desorb the adsorbed $H_2O$ molecules from the clusters; indeed, we find evidence for such processes in our discussion of the $Au_6^+$ cluster (see Section 3.2). The presence of $H_2O$ in the mass spectra for larger cluster sizes suggests that the energy released upon CO adsorption is sufficiently small so that the water desorption barriers are not crossed, with $H_2O$ molecules remaining adsorbed to the cluster.

### 3.2. Coadsorption of CO and $H_2O$ on $Au_6^+$

In this section, we present records of measurements of coadsorption of CO and $H_2O$ on $Au_6^+$ at 300 K, and the results of theoretical calculations that determine the ways that dynamic structural fluxionality and kinetic pathways are expressed in the adsorption reaction data. The theoretical calculations yield: (a) energy barriers that enable dynamic fluxionality between two $Au_6^+$ isomers as a function of the number of both coadsorbed CO and $H_2O$ molecules, and (b) identification of kinetic pathways guiding the formation of $Au_6(CO)_m(H_2O)_p^+$ complexes. These calculations will be shown to explain the observed adsorption mass spectra.

#### 3.2.1. Energy barriers for fluxionality

Measurements of CO adsorption on $Au_6^+$ were performed to enable comparison of mass spectra in the absence of water to spectra obtained in the presence of $H_2O$ coadsorption at identical CO pressures and temperature. Fig. 4a displays the sequence of mass spectra for the saturated adsorption of CO on $Au_6^+$ obtained at 300 K. The optimal structures shown above the mass spectra were calculated for the adsorption complexes identified in the mass spectra. The bare cluster exhibits a triangular structure designated as: $Au_6(t)^+$ [34]. The mass spectrum taken for a reaction time of 1 s is particularly interesting. The intensity of the (6, 3) complex suggests that the adsorption populations are concentrating in this complex as an intermediate saturated level. The triangular structure of this complex, $Au_6(t)(CO)_3^+$, is shown with CO bound to all the preferred apex sites with an average binding energy of 1.21 eV; the adsorption energies of the sequential addition of CO to the cluster (starting with adsorption to the bare cluster, and ending with $[Au_6(t)(CO)_3]^+$) are, respectively: 1.39 eV, 1.25 eV and 1.00 eV (see Table 1). The small peak on the shoulder of the larger (6, 4)

**Table 1**
CO binding energies to the bare $Au_6^+$ cluster, and to the cluster with preadsorbed water $Au_6^+(H_2O)_p$ ($p = 1,2$). The binding energy is calculated as: $BE[CO]_{m,p} = E[Au_6^+ + mCO + pH_2O] + E[CO] - E[Au_6^+(CO)_{m+1}(H_2O)_p]$.

| $m/p$ | 0 $H_2O$ | 1 $H_2O$ | 2 $H_2O$ |
|---|---|---|---|
| 0 CO (first) | 1.39 | 1.26 | 1.02 |
| 1 CO (second) | 1.25 | 1.04 | 0.66 |
| 2 CO (third) | 1.00 | 0.70 | 0.59 |

peak for the $Au_6(CO)_4^+$ complex is identified as $[Au_6(t)(CO)_3H_2O]^+$ in which the water is adsorbed from the residual $H_2O$ background pressure. The intensity of the saturated incomplete hexagonal (ih) adsorption complex $Au_6(ih)(CO)_4^+$ remains unchanged in the mass spectra taken at longer reaction times. The lower panels of the mass spectra in Fig. 4a exhibit a small peak for adsorption of residual $H_2O$ on $Au_6(CO)_4^+$ at the higher reaction time.

Calculations have been performed that yield the transition state energy barriers and final state energies for a transition between complexes formed from the planar isomers $Au_6(t)^+$ and $Au_6(ih)^+$. Additionally, energy barriers were calculated for transitions between the complexes $[Au_6(t)(CO)_m(H_2O)_p]^+ \rightarrow [Au_6(ih)(CO)_m(H_2O)_p]^+$ and they are given in Table 2. Examples of these transitions are displayed in Fig. 5. In Fig. 5b, the calculations reveal that the transition between the $Au_6(t)(CO)_3^+ \rightarrow Au_6(ih)(CO)_3^+$ complexes entails an energy barrier of 0.14 eV, which represents a reduction of 0.24 eV relative to the barrier between bare clusters in Fig. 5a. Whereas for the bare cluster (Fig. 5a) the isomeric structural transformation is endothermic (by 0.19 eV), the isomeric transformation in Fig. 5b is predicted to be exothermic, with the final energy lying 0.24 eV below the initial state. With a calculated barrier of merely 0.14 eV, the structural transition could be assisted by the energy released upon CO adsorption of ~1 eV. The bonding of CO to the gold hexamer cation is found (through Bader charge analysis [44,45]) to be accompanied by transfer of a small amount of electron charge to the gold cluster (0.12e, 0.23e, and 0.41e, for adsorption of 1CO, 2CO and 3CO molecules, respectively, see Fig. S1.4 in the Supplementary data), correlating with the aforementioned reduction in binding energy of the CO molecules (Table 1), and the decreasing trend calculated for the structural transformation barriers: 0.53 eV, 0.30 eV and 0.14 eV corresponding to 1, 2, and 3 adsorbed CO molecules (see Table 2).

As shown in Fig. 5c, the complex formed by the coadsorption of two $H_2O$ molecules, $[Au_6(t)(CO)_3(H_2O)_2]^+$, essentially obliterates the energy barrier and increases the exothermicity to 0.67 eV. The coadsorption of even one $H_2O$ to form $[Au_6(t)(CO)_3H_2O]^+$ is shown in Table 2 to bring about a transition state barrier reduction of 0.11 eV. It is quite possible that the transitions occurring in the mass spectra shown in Fig. 3, $[Au_{16}(CO)_{10}H_2O]^+ \rightarrow [Au_{16}(CO)_{12}(H_2O)_2]^+$, and also in the Supplementary data for $n = 12$, 13, 15 and 18, can be understood as the result of dynamic structural functionality initiated by the adsorption of a single $H_2O$ molecule.

The above-noted correlation between the decrease of the transition state energy barriers and the lowering of the energy of the final state of the structural fluxional transformation (incomplete hexagonal, ih) relative to the initial isomeric state (triangular, t), results in smaller values of the total energy difference between the two states, $\Delta E(t \rightarrow ih) = E(ih) - E(t)$, see Table 2; negative values of $\Delta E(t \rightarrow ih)$ indicate an exothermic structural transformation, see in particular the patterns in the bottom row and the rightmost column of Table 2). Following the Evans–Polanyi principle [46], the final state energy lowering serves as a driving force that promotes (through lowering of the transition state barrier) the occurrence of the fluxional structural transition between the triangular and incomplete hexagonal structures of the $H_2O$/CO adsorption complexes of the gold hexamer cation. The consequent increase in the transition rate is dramatically manifested by comparing the mass spectra in Fig. 4a with those obtained for $H_2O$/CO coadsorption shown in Fig. 4b.

Prior to discussing the observations given in Fig 4a and b we comment on results we obtained through first-principles

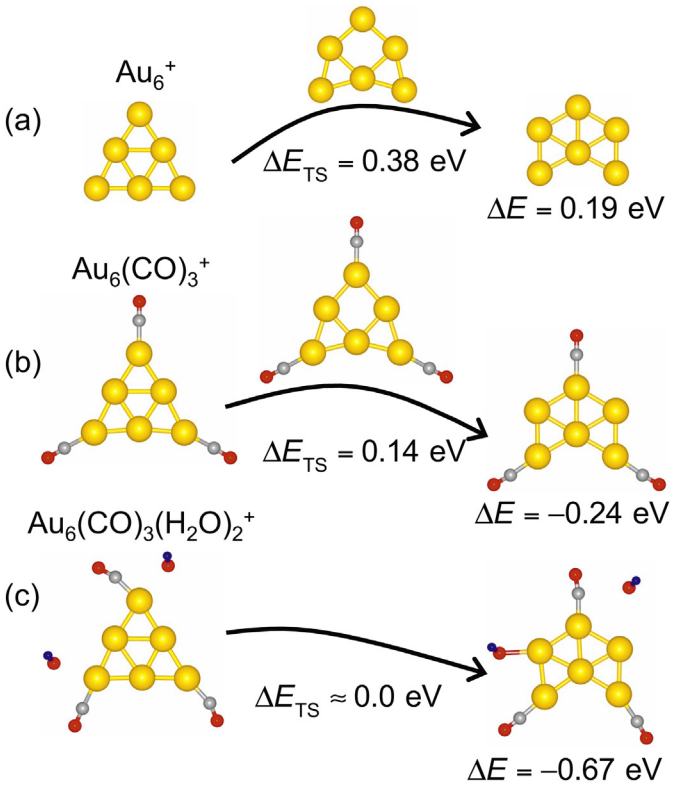


**Fig. 5.** Atomic structures of $Au_6^+$ cluster complexes and transition state energies, obtained from first-principles calculations. (a) Bare clusters exhibiting a transition between the triangular ground state $Au_6(t)^+$ and the incomplete hexagonal isomer $Au_6(ih)^+$ at $\Delta E = 0.19$ eV through a transition state (TS) with a TS barrier $\Delta E_{TS} = 0.38$ eV. (b) Transition of the complex $Au_6(CO)_3^+$ between the triangular $Au_6(t)(CO)_3^+$ and the incomplete hexagonal isomer $Au_6(ih)(CO)_3^+$ at $\Delta E = -0.24$ eV through a TS, with a barrier of $\Delta E_{TS} = 0.14$ eV. (c) Transition of the coadsorption complex $Au_6(CO)_3(H2O)_2^+$ between the triangular cluster $Au_6(t)(CO)_3(H2O)_2^+$ and the incomplete hexagonal Au6(ih)$(CO)_3(H2O)_2^+$ at $\Delta E = -0.67$ eV, occurring through a transition state with a negligible barrier $\Delta E_{TS}$. In these three transitions, the energies are relative to the initial state; positive reaction energies $\Delta E$ correspond to endothermic transitions (a and b), whereas $\Delta E < 0$, indicates an exothermic transition (c). Au atoms are represented by yellow spheres, carbon atoms by gray spheres, and oxygen atoms by red spheres. For inter atomic distances corresponding to the structures shown here, see Fig. S1.3 in the Supplementary data. (For interpretation of the references to color in this figure legend, the reader is referred to the web version of this article.)

**Table 2**
First-principles calculated transition state barriers (and energy balance $\Delta E(t \rightarrow ih) = E(ih) - E(t)$, in brackets) for fluxional structural transformations from triangular (t) to incomplete hexagonal (ih) structural isomers of $Au_6^+(CO)_m(H2O)_p$, $m = 0$–3, $p = 0$–2, in eV units. A negative value of $\Delta E(t \rightarrow ih)$ corresponds to an exothermic transformation. Note in particular the correlation between the lowering of the transformation barrier for $Au_6^+(CO)_3(H_2O)_p$ ($p = 0$–2) with increasing $H_2O$ adsorption (e.g., bottom row, left to right), as well as for $Au_6^+(CO)_m(H_2O)_2$ ($m = 0$–3) with increasing CO adsorption (last column, top to bottom), and for increasing CO coverage with no adsorbed water, i.e., see first column (0 $H_2O$), $Au_6^+(CO)_m$ ($m = 1$–3).

| $m/p$ | 0 $H_2O$ | 1 $H_2O$ | 2 $H_2O$ |
|---|---|---|---|
| 0 CO | 0.38 (0.19) | 0.51 (0.34) | 0.55 (0.39) |
| 1 CO | 0.53 (0.51) | 0.44 (0.25) | 0.32 (0.10) |
| 2 CO | 0.30 (0.05) | 0.18 (−0.06) | 0.22 (0.18) |
| 3 CO | 0.14 (−0.24) | 0.11 (−0.50) | ~0.0 (−0.67) |

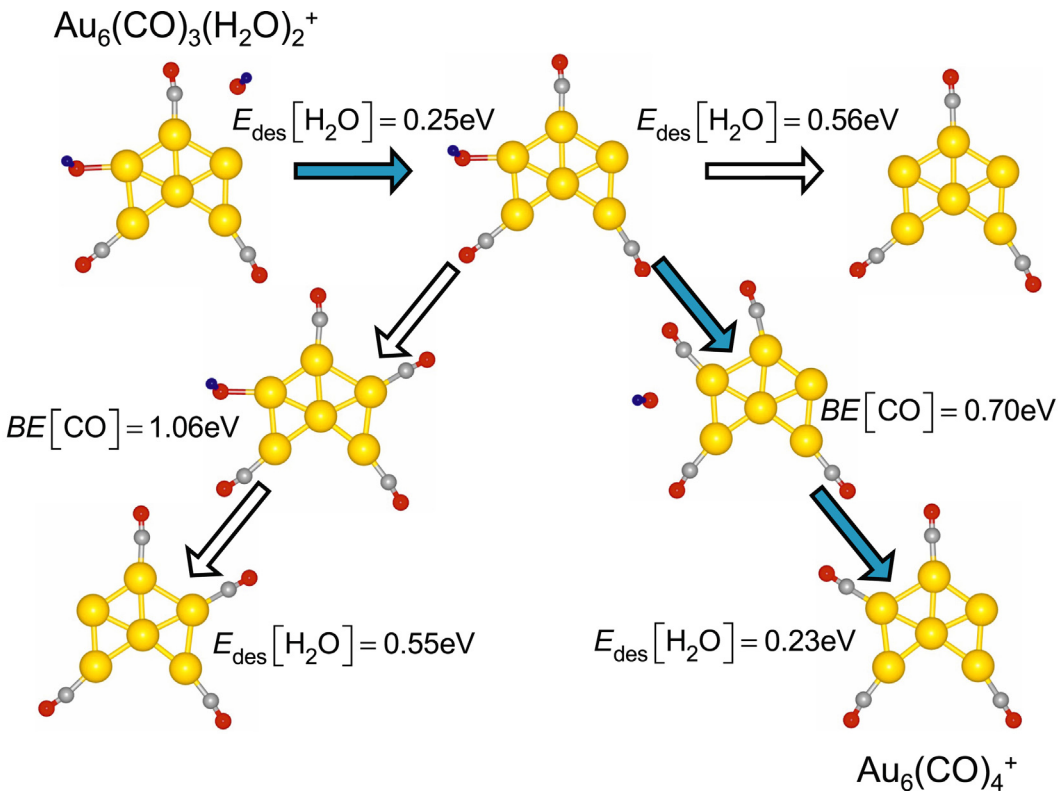


**Fig. 6.** Kinetic pathways for transition between $[Au_6(CO)_3(H_2O)_2]^+$ and the complex $Au_6(CO)_4^+$. The blue arrows identify a minimum energy kinetic pathway for the reaction that involves (starting from the initial complex in the top left): adsorption of a CO molecule and desorption of two $H_2O$ molecules, resulting in the experimentally observed complex, shown at the bottom right. A couple of alternative pathways are denoted by white-hollow arrows – one of these pathways (going at the top horizontally from left to right) does not result in the desired product, and the other (going diagonally to the bottom left) entails a larger activation energy than the optimal pathway.

calculations for $H_2O$ and CO coadsorption on the ground state (triangular structure) of the gold hexamer cation. First we note that the adsorption of an $H_2O$ molecule on the bare $Au_6^+$ cluster occurs at an apex site of the triangle with a relatively large binding energy of 0.98 eV. Adsorption of a second water molecule at another apex, occurs with a binding energy of 0.85; we note that dissociation of an adsorbed $H_2O$ molecule is unlikely since, depending on the adsorption site of the H atom (with the OH being adsorbed at the apex of the triangle), these dissociation processes entail an energy increase of 2.09 eV (for H adsorbed on a gold atom located on the side of the triangle) or 2.47 eV (for adsorption of the H at an apex site of the triangle). In comparison with the relatively strong binding of $H_2O$ molecules to the bare $Au_6^+$ cluster, water adsorption on the cluster with preadsorbed CO (i.e., $Au_6(CO)_3^+$) leads to weak binding; 0.34 eV of the first $H_2O$ molecule and 0.12 eV for the second one. However, reversing the order of exposure, that is, CO adsorbing on the gold cluster with preadsorbed water, e.g., $Au_6^+(H_2O)_2$ (see Table 1, rightmost column), the sequential adsorption of CO occurs with binding energies of the adsorbing molecules that are no less than 0.59 eV (i.e., 1.02 eV for the first CO molecule, 0.66 eV for the second, and 0.59 for the third). Although the same final cluster complex is reached, i.e., $Au_6(t)(CO)_3H_2O]^+$, independent of the order of exposure, the above theoretical results suggest a kinetic advantage to the adsorption sequence where water is adsorbed prior to CO (as indeed has been done in our experiments, see below).

In the experimental sequence used to obtain the mass spectra, the cluster ions are first exposed to the seeded water vapor flow for a given reaction time, $\tau_{H_2O}$, and subsequently these clusters are immediately exposed to the CO flow for a shorter reaction time, $\tau_{CO}$, at the same pressure used to obtain data in Fig. 4a. Most surprising is the rapidity that the saturated adsorption of CO is achieved following the $H_2O$ exposure, resulting in a saturation level identical to that found in the absence of water (Fig. 4a). Because evacuation of the chamber to background pressures is performed after the acquisition of each mass spectrum, it is irrelevant that a $\tau_{H_2O} = 60$s reaction time was the initial value. Since a similar mass spectrum is obtained for $\tau_{H_2O} = 1$s and 60s, this time does not appear to be a particularly sensitive parameter. The dominating presence of the saturation complex $Au_6(ih)(CO)_4^+$ in the mass spectra is obtained for a CO reaction time of 0.3 s in the presence of $H_2O$. The identical saturated complex is observed for a CO reaction time $\tau_{CO} = 5$ s without the presence of $H_2O$. This ratio of reaction times could be fine tuned by obtaining additional mass spectra, but the more important point is the occurrence of a significant increase in the CO saturated adsorption rate following the $H_2O$ reaction time.

### 3.2.2. Kinetic pathways

The DFT calculations revealed that the presence of $H_2O$ is required to provide a very rapid transition to the complex $[Au_6(ih)(CO)_3(H_2O)_2]^+$ reflected in a significant lowering of the transition state barrier for the isomeric transformation. However, the mass spectra in Fig. 4b indicate that the final complex obtained for saturated adsorption does not include adsorbed $H_2O$ molecules. The calculated reaction pathway, indicated by the blue arrows in Fig. 6, includes the reaction complexes found in the adsorption mass spectra shown in Fig. 4b. The identified pathway entails the desorption of relatively weakly bound $H_2O$ molecules from complexes of the gold hexamer cation, see Fig. 6. In the first complex, $[Au_6(ih)(CO)_3(H_2O)_2]^+$ (top left in Fig. 6) the average binding energy of CO to the cluster is BE[CO] = 0.76 eV, and desorption energy of one of the coadsorbed $H_2O$ molecules is $E_{des}[H_2O] = 0.25$ eV. In the second complex, $[Au_6(ih)(CO)_4H_2O]^+$

(third complex along the blue arrow chain) BE[CO] = 0.70 eV and $E_{des}[H_2O]$ = 0.23 eV. Desorption of the weakly bound $H_2O$ from the first complex could result from the energy released upon the adsorption of up to three CO molecules, whereas in the second complex, the desorption of the $H_2O$ molecule may be assisted by the energy released upon the adsorption of a single CO molecule [47]. As a result, on average, the second complex will be formed more slowly and this would account for the presence of peaks for both complexes, $[Au_6(ih)(CO)_4]^+$ and $[Au_6(ih)(CO)_4H_2O]^+$, in the mass spectra shown in Fig. 4. It should be noted that saturated adsorption at 150 K is observed for the $[Au_6(CO)_6]^+$ complex as shown in Fig. 1, a result that is also suggested by previous studies [33]. Our results for the saturated complex $[Au_6(CO)_4]^+$ at 300 K in Fig. 4a and 4b suggest that two of the six CO molecules in $[Au_6(CO)_6]^+$ are weakly bound, requiring lower temperatures to be observed.

## 4. Summary

Experiments were performed to measure saturated adsorption on gold cluster cations held in a quadrupole ion trap and exposed to reactant gases. Although the primary emphasis of this paper is the study of coadsorbed CO and $H_2O$ at 300 K, results for saturated adsorption of CO on $Au_5^+$ and $Au_{16}^+$ at 150 K are first presented to characterize the adsorption processes that can be observed in mass spectra.

Coadsorption measurements of $H_2O$ and CO on $Au_6^+$ at 300 K were analyzed with the use of theoretical first-principles (DFT) calculations to provide insights for the coadsorption reaction mechanisms. The coadsorption mass spectra obtained as a function of reaction time and reactant pressures indicated an increase in the rate for saturated adsorption by an order of magnitude (compared to the rate of adsorption of the individual reactants). The computations revealed that the presence of $H_2O$ induces a very rapid transition between different structures of the complex $[Au_6(CO)_3(H_2O)_2]^+$ by reducing the transition state barrier to a negligible value, and increasing the reaction exothermicity by 0.43 eV relative to its value in the absence of water. The lowering of both transition state energy barriers and the final state energies presents a strong driving force for fluxionality of the transition between the $Au_6^+$ complex structures. Calculated kinetic pathways demonstrate that this rapid transition leads to an acceleration of the adsorption rate, yielding the saturated complex masses identified in the mass spectra.

The combination of experiment and theoretical calculations provide insights about the saturated adsorption processes operative in the presence of coadsorbed CO and $H_2O$ on $Au_6^+$ clusters. These calculations also elucidate the saturated adsorption for a wider range of cluster sizes, having 12–18 atoms, observed in the presence of adsorbed $H_2O$.

## Acknowledgements

J.H.P. gratefully acknowledges helpful discussions with Dr. James Foley (Rowland) and Dr. Michael Burns (Rowland) and the generous financial support by the U.S. Department of Energy (DOE) under Grant DE-FG02-061ER45921. The work of R.N.B. at the Georgia Institute of Technology was supported by a grant from the US Air Force Office of Scientific Research, and the work of U.L. was supported in part by a grant from the Office of Basic Energy Sciences of the US Department of Energy under Contract No. FG05-86ER45234. Calculations were performed at the Georgia Institute of Technology Center for Computational Materials Science.

## Appendix A. Supplementary data

Supplementary data associated with this article can be found, in the online version, at http://dx.doi.org/10.1016/j.ijms.2014.07.006.

## References

[1] (a) M. Haruta, CATTECH 6 (2002) 102;
(b) M. Haruta, Chem. Record 3 (2003) 75.
[2] M. Chen, D.W. Goodman, Acc. Chem. Res. 39 (2006) 739.
[3] C. Louis, D.T. Thompson, G.C. Bond, Catalysis by Gold, Imperial College Press, London, 2006.
[4] (a) T.M. Bernhardt, U. Heiz, U. Landman, in: U. Heiz, U. Landman (Eds.), Nanocatalysis, Springer-Verlag, Berlin, 2007, pp. 1–191 Chapter 1;
(b) U. Landman, B. Yoon, C. Zhang, U. Heiz, M. Arenz, Top. Catal. 44 (2007) 145.
[5] G.J. Hutchings, M. Brust, H. Schmidbaur, Chem. Soc. Rev. 37 (2008) 1759.
[6] M. Haruta, T. Kobayashi, H. Sano, N. Yamada, Chem. Lett. 34 (405) (1987).
[7] M. Haruta, Chem. Express 5 (1988) 349.
[8] M. Haruta, N. Yamada, T. Kobayashi, S. Iijima, J. Catal. 115 (1989) 301.
[9] M. Haruta, T. Takase, T. Kobayashi, S. Tsubota, in: S. Yoshida, N. Takezawa, T. Ono (Eds.), Catalytic Science and Technology, vol. 1, Kodansha, Tokyo, 1991.
[10] M. Daté, M. Haruta, J. Catal. 201 (2001) 221.
[11] M. Daté, Y. Ichihashi, T. Yamashita, A. Chiorino, F. Boccuzzi, M. Haruta, Catal. Today 72 (2002) 89.
[12] M. Daté, M. Okumura, S. Tsubota, M. Haruta, Angew. Chem. Int. Ed. 43 (2004) 2129.
[13] M. Valden, X. Lai, D.W. Goodman, Science 281 (1998) 1647.
[14] F.T.E. Gao Wood, D.W. Goodman, Catal. Lett. 134 (2010) 9.
[15] T. Yan, J. Gong, D.W. Flaherty, C.B. Mullins, J. Phys. Chem. 115 (2011) 2057.
[16] (a) U. Heiz, A. Sanchez, S. Abbet, W.-D. Schneider, J. Am. Chem. Soc. 121 (1999) 3214;
(b) U. Heiz, A. Sanchez, S. Abbet, W.-D. Schneider, Chem. Phys. 262 (2000) 189.
[17] (a) R.N. Barnett, U. Landman, Phys. Rev. B 48 (1993) 2081;
(b) U. Landman, Proc. Natl. Acad. Sci. U. S. A. 102 (2005) 6671.
[18] (a) M. Moseler, H. Häkkinen, U. Landman, Phys. Rev. Lett. 89 (2002) 033401;
(b) X.P. Xing, B. Yoon, U. Landman, J.H. Parks, Phys. Rev. B 74 (2006) 165423;
(c) B. Yoon, P. Koskinen, B. Huber, O. Kostko, B. Von Issendorff, H. Häkkinen, M. Moseler, U. Landman, Chem. Phys. Chem. 8 (2007) 157.
[19] A. Sanchez, S. Abbet, U. Heiz, W.-D. Schneider, H. Häkkinen, R.N. Barnett, U. Landman, J. Phys. Chem. A 103 (1999) 9573.
[20] H. Häkkinen, S. Abbet, A. Sanchez, U. Heiz, U. Landman, Angew. Chem. Int. Ed. 42 (2003) 1297.
[21] B. Yoon, H. Häkkinen, U. Landman, A.S. Worz, J.-M. Antonietti, S. Abbet, K. Judai, U. Heiz, Science 307 (2005) 403.
[22] A. Bongiorno, U. Landman, Phys. Rev. Lett. 95 (2005) 106102.
[23] (a) D. Ricci, A. Bongiorno, G. Pacchioni, U. Landman, Phys. Rev. Lett. 97 (2006) 36106;
(b) B. Yoon, C. Zhang, U. Heiz, M. Arenz, J. Am. Chem. Soc. 129 (2007) 2229;
(c) C. Harding, V. Habibpour, S. Kunz, A. Nam-Su Farnbacher, U. Heiz, B. Yoon, U. Landman, J. Am. Chem. Soc. 131 (2009) 538;
(d) B. Yoon, C. Zhang, U. Landman, Phys. Rev. Lett. 100 (2008) 056102.
[24] (a) S.M. Lang, T.M. Bernhardt, R.N. Barnett, U. Landman, Angew. Chem. Int. Ed. 49 (2010) 980;
(b) S.M. Lang, T.M. Bernhardt, R.N. Barnett, U. Landman, J. Phys. Chem. 115 (2011) 6788;
(c) S.M. Lang, T.M. Bernhardt, R.N. Barnett, B. Yoon, U. Landman, J. Am. Chem. Soc. 131 (2009) 8939.
[25] A.A. Herzing, C.J. Kiely, A.F. Carley, P. Landon, G.J. Hutchings, Science 321 (2008) 1331.
[26] M.J. Manard, P.R. Kemper, M.T. Bowers, J. Am. Chem. Soc. 127 (2005) 9994.
[27] L. Barrio, P. Liu, J.A. Rodríguez, J.M. Campos-Martín, J.L.G. Fierro, J. Chem. Phys. 125 (2006) 164715.
[28] R. Pal, W. Huang, Y.-L. Wang, H.-S. Hu, S. Bulusu, X.-G. Xiong, J. Li, L.-S. Wang, X.C. Zeng, J. Phys. Chem. Lett. 2 (2011) 2288.
[29] R. Mitric, C. Burgel, V. Bonacic-Koutecky, Proc. Natl. Acad. Sci. U. S. A. 104 (2007) 10314.
[30] R.O. Ramabhadran, E.L. Becher III, A. Chowdhury, K. Raghavachari, J. Phys. Chem. A 116 (2012) 7189.
[31] K.P. Kerns, E.K. Parks, S.J.J. Riley, Chem. Phys. 112 (2000) 3394.
[32] M. Neumaier, F. Weigend, O. Hampe, M.M. Kappes, J. Chem. Phys. 122 (2005) 104702.
[33] A. Fielicke, G. von Helden, G. Meijer, D.B. Pedersen, B. Simard, D.M. Rayner, J. Am. Chem. Soc. 127 (2005) 8416.
[34] S. Gilb, P. Weis, F. Furche, R. Ahlrichs, M.M. Kappes, J. Chem. Phys. 116 (2002) 4094.
[35] I. Fleischer, D.M. Popolan, M. Krstic, V. Bonacic-Koutecky, T.M. Bernhardt, Chem. Phys. Lett. 565 (2013) 74.
[36] (a) X. Xing, R.M. Danell, I.L. Garzón, K. Michaelian, M.N. Blom, M.M. Burns, J.H. Parks, Phys. Rev. B 72 (2005) 081405;
(b) J.H. Parks, X. Xing, in: D. Woodruff (Ed.), Atomic Clusters: From Gas Phase to Deposited, vol. 12, Elsevier, 700 New York, 2007.
[37] S.M. Lang, T.M. Bernhardt, Eur. Phys. J. D 52 (2009) 139.

[38] (a) R.E. March, J. Mass Spectrom. 32 (1997) 351;
(b) J.D. Williams, K.A. Cox, R. Graham Cooks, S.A. McLuckey, K.J. Hart, D.E. Goeringer, Anal. Chem. 66 (1994) 725.
[39] N. Troullier, J.L. Martins, Phys. Rev. B 43 (1991) 1993.
[40] J.P. Perdew, K. Burke, M. Ernzerhof, Phys. Rev. Lett. 77 (1996) 3865.
[41] D.M. Popolan, M. Noßler, R. Mitric, T.M. Bernhardt, V. Bonacic-Koutecky, Phys. Chem. Chem. Phys. 12 (2010) 7865.
[42] H.-J. Zhai, L.-L. Pan, B. Dai, B. Kiran, J. Li, L.-S. Wang, J. Phys. Chem. C 112 (2008) 11920.
[43] H. Häkkinen, U. Landman, Phys. Rev. B 62 (2000) R2287.
[44] R.W.F. Bader, Atoms in Molecules: A Quantum Theory, Oxford University Press, New York, 1990.
[45] W. Tang, E. Sanville, G. Henkelman, J. Phys. Condens. Matter 21 (2009) 084204.
[46] (a) J. Horiuti, M. Polanyi, Acta Physicochim. U.R.S.S. 2 (1935) 505;
(b) R.A. Ogg, M. Polanyi, Trans. Faraday Soc. 31 (1935) 604;
R.A. Ogg, M. Polanyi, Trans. Faraday Soc. 31 (1935) 1375;
(c) M.G. Evans, M. Polanyi, Trans. Faraday Soc. 32 (1936) 1340;
(e) R.P. Bell, Proc. R. Soc. A 154 (1936) 414.
[47] G.E. Johnson, N.M. Reilly, E.C. Tyo, A.W. Castleman Jr., J. Phys. Chem. C 112 (2008) 9730.